Examination of Protonation-Induced Dinitrogen Splitting by in Situ EXAFS Spectroscopy

Abbenseth, Josh; Oudsen, Jean-Pierre H; Venderbosch, Bas; Demeshko, Serhiy; Finger, Markus; Herwig, Christian; Würtele, Christian; Holthausen, Max C; Limberg, Christian; Tromp, Moniek

Published in:
Inorganic Chemistry

DOI:
10.1021/acs.inorgchem.0c02134

Inorganic Chemistry

pubs.acs.org/IC Article

Examination of Protonation-Induced Dinitrogen Splitting by *in Situ* EXAFS Spectroscopy

Josh Abbenseth, Jean-Pierre H. Oudsen,[#] Bas Venderbosch,[#] Serhiy Demeshko, Markus Finger, Christian Herwig, Christian Würtele, Max C. Holthausen, Christian Limberg, Moniek Tromp,[*] and Sven Schneider[*]

Cite This: *Inorg. Chem.* 2020, 59, 14367−14375 Read Online

ACCESS | Metrics & More | Article Recommendations | Supporting Information

ABSTRACT: The splitting of dinitrogen into nitride complexes emerged as a key reaction for nitrogen fixation strategies at ambient conditions. However, the impact of auxiliary ligands or accessible spin states on the thermodynamics and kinetics of N−N cleavage is yet to be examined in detail. We recently reported N−N bond splitting of a {Mo(μ^2:η^1:η^1-N_2)Mo}-complex upon protonation of the diphosphinoamide auxiliary ligands. The reactivity was associated with a low-spin to high-spin transition that was induced by the protonation reaction in the coordination periphery, mainly based on computational results. Here, this proposal is evaluated by an XAS study of a series of linearly N_2 bridged Mo pincer complexes. Structural characterization of the transient protonation product by EXAFS spectroscopy confirms the proposed spin transition prior to N−N bond cleavage.

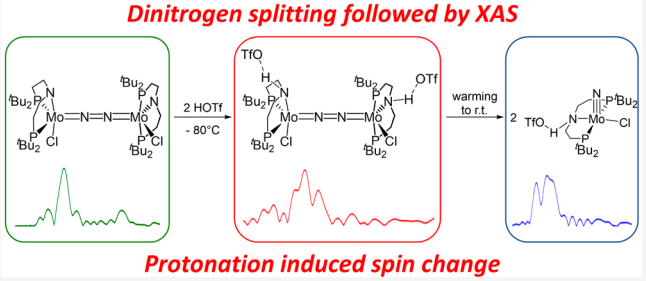

INTRODUCTION

For around 100 years, industrial ammonia production has been carried out at high temperatures and pressures by the heterogeneously catalyzed Haber-Bosch process (HBP).[1] Efficient, synthetic N_2 fixation at ambient conditions, as

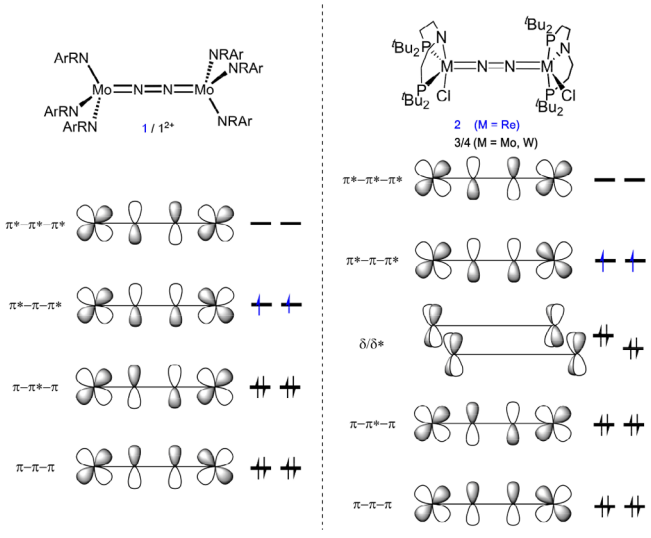

Figure 1. Qualitative MO splitting diagrams for tetrahedrally and square-pyramidally coordinated precursors to N_2 splitting (R = $C(CD_3)_2CH_3$, Ar = 3,5-$C_6H_3Me_2$).[6,8,9]

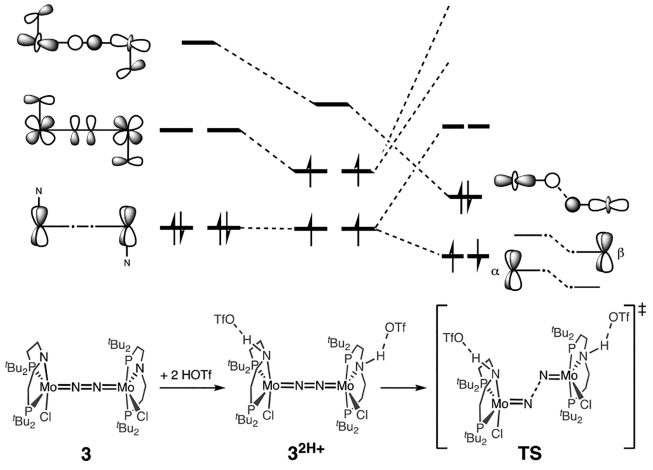

Figure 2. Qualitative MO splitting diagram for protonation-induced N−N splitting of **3** via pincer protonated intermediate $\mathbf{3}^{2H+}$ and transition state **TS**.[9]

Received: July 17, 2020
Published: September 22, 2020

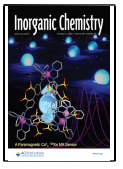

https://dx.doi.org/10.1021/acs.inorgchem.0c02134
Inorg. Chem. 2020, 59, 14367−14375

mediated by the enzyme nitrogenase, still represents a major challenge due to the high kinetic and thermodynamic stability of N_2.[2] The HBP proceeds via initial dissociative chemisorption of N_2.[1] This mechanism differs fundamentally from the PCET based pathway of nitrogenase and most molecular catalysts.[3,4] Nishibayashi and co-workers recently proposed a HBP-related, dissociative mechanism for homogeneous Mo catalysts that commences with full N−N bond cleavage into terminal nitride complexes,[5] which renewed the interest in N_2 splitting as a strategy to N_2 fixation. After the pioneering work of Laplaza and Cummins,[6] several examples have been reported.[7] However, robust predictors for N_2 splitting reactivity are yet to be developed.

M−N bonding considerations for linearly N_2 bridged complex **1** (Figure 1) provide a simple basis to rationalize the reactivity vs thermal stability of $\mathbf{1}^+$ and $\mathbf{1}^{2+}$.[6b] Formation of the terminal nitride $[Mo(N)(NRAr)_3]$ was associated with an electronic triplet $(\pi-\pi-\pi)^4(\pi-\pi^*-\pi)^4(\pi^*-\pi-\pi^*)^2$ $(=\pi^{10})$ ground-state configuration of the {Mo−N−N−Mo} core. *Zigzag* distortion leads to crossing onto the N−N dissociative singlet surface via electronic rearrangement from the $(\pi^*-\pi-\pi^*)$-derived levels into an N−N σ^*-MO. This simple picture could be transferred to linearly N_2 bridged complexes in other coordination geometries that split into terminal nitrides.[7] For example, the $(\pi^{10}\delta^4)$ complex $[(N_2)\{ReCl(PNP)\}_2]$ (**2**, Figure 1) undergoes facile N−N scission, while the isostructural $(\pi^8\delta^4)$ complexes $[(N_2)\{MCl(PNP)\}_2]$ (M = Mo (**3**), W (**4**)) are thermally stable.[8−10]

We recently reported that the protonation of **3** at the pincer nitrogen triggers decay into Mo^V nitride $[Mo(N)Cl(HPNP)]^+$ (**5**).[9] The striking protonation-induced reduction of the kinetic barrier for N−N cleavage was attributed to singlet ground-state destabilization and population of a $(\pi^{10}\delta^2)$ quintet state for $[(N_2)\{MCl(HPNP)\}_2]^{2+}$ ($\mathbf{3}^{2H+}$, Figure 2). N−N scission was therefore associated with an auxiliary ligand effect that results from mixing of the amido ligands of **3** with the π- and σ-MO manifold of the Mo−N−N−Mo core. This interpretation strongly relied on computational modeling as the paramagnetic and thermally unstable intermediate $\mathbf{3}^{2H+}$ eluded structural characterization by X-ray diffraction (XRD).

Mo K-edge X-ray absorption spectroscopy (XAS) is a valuable spectroscopic tool for the structural characterization of molecular coordination compounds and metalloenzymes like nitrogenase.[11] In the context of molybdenum mediated N_2 splitting, Laplaza et al. and very recently Yamamoto et al. examined transient intermediates by Mo K-edge XAS.[6b,12] We here report an *in situ* XAS study to evaluate our previous structural and electronic assignment for $\mathbf{3}^{2H+}$.

EXPERIMENTAL SECTION

Synthetic and Analytical Details. All experiments were carried out under inert conditions using standard Schlenk and glovebox techniques (argon atmosphere). Solvents were purchased in HPLC quality and dried using an MBraun Solvent Purification System, except PhCl which was dried over CaH_2 for 1 week and distilled. Deuterated solvents were obtained from Euriso-Top GmbH and dried over Na/K (THF-d_8) and CaH_2 (CD_2Cl_2). $AgBF_4$, $AgSbF_6$, $^{15}N_2$, HOTf (Sigma-Aldrich), and $Ag[Al(OR_F)_4]$ (Iolitec) were used as purchased. **3** and **5** were prepared as previously reported.[9] Experimental EPR spectra were recorded on a Bruker ELEXSYS-II E500 CW-EPR. The spectra were simulated by iteration of the isotropic *g* values, hyperfine interaction coupling constants, and line widths using EasySpin.[13] Magnetic susceptibility measurements were performed with a Quantum Design MPMS-XL SQUID magnetometer in the temperature range from 295 to 2 K at 0.5 T applied. The powdered sample was contained in a Teflon bucket and fixed in a nonmagnetic sample holder. Each raw data point for the measured magnetic moment of the sample was corrected for the diamagnetic contribution by subtraction of the experimentally determined magnetic measurement of the Teflon bucket. The molar susceptibility data were corrected for the diamagnetic contribution using the Pascal constants and the increment method according to Haberditzl.[14] Experimental data were modeled with the julX program.[15] Elemental analyses were obtained from the analytical laboratories at the Georg-August University on an Elementar Vario EL 3. NMR spectra were recorded on a Bruker Avance III and were calibrated to the residual solvent proton resonance (THF-d_8 = 3.58 ppm, CD_2Cl_2 = 5.32 ppm). Raman spectra were recorded in THF solution at −100 °C using a Triple Raman Spectrometer TR 557 from S&I (Spectroscopy & Imaging GmbH). An argon ion laser with a wavelength of 514.5 nm and a power of 100 mW was used for excitation.

Synthesis of $[\{MoCl(PNP)\}_2(\mu\text{-}N_2)][Al(OR_F)_4]$ (3-$Al(OR_F)_4$). **3** (10.2 mg, 10.1 μmol, 1.00 equiv) and $Ag[Al(OR_F)_4]$ (10.8 mg, 10.1 μmol, 1.00 equiv) were dissolved in benzene and stirred for 16 h at room temperature. The solution was filtered, and the residue was extracted with benzene (15 × 2 mL). The solvent was removed, and the residue was dissolved in PhCl (2 mL), layered with pentane, and stored at −35 °C for 2 days. The precipitate was washed with pentane/benzene (1:1, 3 × 3 mL) and extracted with PhCl (4 × 2 mL). After removal of the solvent, **3**-$Al(OR_F)_4$ was obtained as a dark brown powder (17.5 mg, 8.84 μmol, 88%). Anal. Calcd for $C_{56}H_{88}AlCl_2F_{36}Mo_2N_4O_4P_4$ (1978.98): C, 34.0; H, 4.48; N, 2.28. Found: C, 34.0; H, 4.68; N; 1.44. Like for parent **3**, the low N value was attributed to a loss of dinitrogen during combustion analysis.[9] NMR (THF-d_8, r.t): ^{1}H (300 MHz) δ = 2.66 (br, 18 H, $PC(CH_3)_3$), 2.41−1.98 (br, 54 H, $PC(CH_3)_3$), −2.59 (br, 2 H), −4.02 (br, 4 H), −4.71 (br, 2 H), −24.08 (br, 2 H), −30.97 (br, 2 H), −32.32 (br, 2 H), −35.7 (br, 2 H). Single crystals suitable for X-ray diffraction were obtained upon reacting **3** with 1 equiv of $AgBF_4$ in THF and successive filtration and vapor diffusion of pentane at −35 °C.

Synthesis of $[\{MoCl(PNP)\}_2(\mu\text{-}N_2)][Al(OR_F)_4]_2$(3-$(Al(OR_F)_4)_2$). **3** (12.5 mg, 12.4 μmol) and $Ag[Al(OR_F)_4]$ (25.2 mg, 23.5 μmol, 1.90 equiv) were dissolved in benzene and stirred for 16 h at room temperature. The solution was filtered and washed with benzene (5 × 2 mL), and the residue was extracted with DCM (3 × 2 mL). The solution was concentrated, layered with toluene, and stored at −80 °C for 2 days. The crude product was filtered, washed with benzene (2 × 2 mL), and extracted with DCM (2 × 2 mL). The solution was filtered through a Celite pad and dried. **3**-$(Al(OR_F)_4)_2$ was obtained as a brown powder (25.0 mg, 8.48 μmol, 69%). Anal. Calcd for $C_{72}H_{88}Al_2Cl_2F_{72}Mo_2N_4O_8P_4$ (2946.08): C, 29.4; H, 3.01; N, 1.90. Found: C, 29.2; H, 3.30; N, 1.66. NMR (CD_2Cl_2, r.t): ^{1}H (300 MHz) δ = 3.81 (br, 18 H, $PC(CH_3)_3$), 3.58−2.88 (br, 54 H, $PC(CH_3)_3$), −5.46 (br, 2 H), −13.1 (br, 2 H), −15.8 (br, 2 H), −58.9 (br, 2 H), −71.3 (br, 2 H), −83.1 (br, 2 H), −88.6 (br, 2 H). Single crystals suitable for X-ray diffraction were obtained upon reacting **3** with 2 equiv of $AgSbF_6$ in THF, filtration, and vapor diffusion of pentane at −35 °C.

Crystallographic Details. Suitable single crystals for X-ray structure determination were selected from the mother liquor under an inert gas atmosphere and transferred in protective perfluoro polyether oil on a microscope slide. The selected and mounted crystals were transferred to the cold gas stream on the diffractometer. The diffraction data were obtained at 100 K on a Bruker D8 three-circle diffractometer, equipped with a PHOTON 100 CMOS detector and an INCOATEC microfocus source with Quazar mirror optics (Mo−K_α radiation, λ = 0.71073 Å). The data obtained were integrated with SAINT, and a semiempirical absorption correction from equivalents with SADABS was applied. The structure was solved and refined using the Bruker SHELX 2014 software package.[16] All non-hydrogen atoms were refined with anisotropic displacement parameters. All C−H hydrogen atoms were refined isotropically on calculated positions by using a riding model with their U_{iso} values

https://dx.doi.org/10.1021/acs.inorgchem.0c02134
Inorg. Chem. 2020, 59, 14367−14375

constrained to 1.5 U_{eq} of their pivot atoms for terminal sp^3 carbon atoms and 1.2 times for all other atoms.

Computational Details. All calculations were performed within the ORCA program suite.[17] The optimization of the molecular structures was carried out using the PBE0[18] functional, Grimme's dispersion correction with Becke-Johnson damping (D3(BJ)),[19] and the chain of spheres (RIJCOSX)[20] approximation to minimize computational costs. Ahlrichs' revised def2-SVP basis set and the corresponding auxiliary basis set were used with an all-electron basis for all elements but Mo for which a Stuttgart-Dresden 28 electron core potential replaced the inner shell 1s-3d orbitals.[21] Tight convergence criteria in the SCF and geometry optimization procedures and a fine integration grid (Grid 5 and GRIDX5) were applied in all calculations. The full molecular systems were evaluated, no symmetry restrains were imposed, and the optimized (gas phase) structures were characterized as minima by analytical vibrational analyses. The electronic structure of $\mathbf{3}^{2+}$ with high-spin electronic configuration was re-evaluated by the broken symmetry protocol, and the geometry was reoptimized within this approach. The energy of an open shell singlet (OSS) BS(1,1) was estimated from the energy ε_{BS} of the optimized single-determinant broken symmetry BS(1,1) solution and the energy ε_{HS} from a separate unrestricted triplet (M_s = 1) high-spin calculation at the same geometry with the same functional and basis set, using the approximate spin correction formula proposed by Yamaguchi:[22]

$$\varepsilon_S = \frac{S_{HS}^2\varepsilon_{LS} - S_{LS}^2\varepsilon_{HS}}{S_{HS}^2 - S_{LS}^2}$$

The antiferromagnetic coupling constant can be estimated accordingly by

$$J = 2.1947\cdot10^5\ \mathrm{cm}^{-1}\cdot\frac{\varepsilon_{LS} - \varepsilon_{HS}}{S_{HS}^2 - S_{LS}^2}$$

The energies of the electronic isomers were evaluated by single point calculations applying the M06 functional,[23] Ahlrichs' def2-TZVPP basis set for all atoms, replacing the 28 core electrons of Mo, and Truhlar's SMD solvation model (THF).[24] Finally, thermodynamic data were computed by applying Grimme's quasi-RRHO approach.[25] The redox potentials were evaluated as described previously for the **4**/$\mathbf{4}^+$/$\mathbf{4}^{2+}$ redox series.[10]

X-ray Absorption Spectroscopy. Mo K-edge XAS measurements were performed at B18 (Diamond) in Didcot, United Kingdom (experimental number SP22432). All measurements were performed in transmission mode. Samples were kept inside a glass, airtight NMR tube under an argon atmosphere. The contents of the THF solution were kept frozen by partial submersion of the NMR tube in liquid nitrogen. Additional cooling was provided by a Cryojet set to 100 K. A single measurement required 3 min; a minimum of 30 scans was required to obtain good signal-to-noise in the data. All acquired spectra were calibrated to a Mo foil. XAS data processing was performed in Athena, and EXAFS analysis was performed in Artemis.[26] The amplitude reduction factor was determined using the Mo foil and was found to be 0.95.

In Situ Protonation of **3**. A *J*-Young NMR tube was filled with **3** (11.1 mg, 10.9 μmol, 1.00 equiv), and THF (0.3 mL) was carefully added directly on top of the substance. After that, HOTf (2.0 μL, 23 μmol, 2.1 equiv) was placed as a drop at the top of the tube. After cooling to −40 °C, the tube was shaken for 2 min at −40 °C. After that, the tube was transferred to the spectrometer and emerged in liquid nitrogen.

RESULTS AND DISCUSSION

Synthesis and Characterization of the Redox Series $[(N_2)]\{MoCl(PNP)\}_2]^{n+}$ (n = 0−2). To carry out *in situ* EXAFS characterization for transient $\mathbf{3}^{2H+}$, we first strived at generating a structurally related and well-defined set of reference compounds. As previously reported,[9] complex **3** exhibits two reversible oxidation waves in the cyclic voltammogram at $E_{1/2}$ = −1.14 and −0.64 V (vs $FeCp_2^+/FeCp_2$), respectively. In comparison to the analogous tungsten complex **4**, these potentials are anodically shifted by approximately 250 mV, which is consistent with metal centered redox events. For the redox series **4** ($\pi^8\delta^4$)/$\mathbf{4}^+$ ($\pi^8\delta^3$)/$\mathbf{4}^{2+}$ ($\pi^8\delta^2$), this was confirmed by spectroscopic, magnetic, and computational characterization, supporting the simple MO picture in Figure 1.[10] In analogy to tungsten, the chemical oxidation of **3** with 1 or 2 equiv of $Ag[Al(OR_F)_4]$ (R_F = $C(CF_3)_3$) in the dark affords the one-electron and two-electron oxidized products $\mathbf{3}^+$ and $\mathbf{3}^{2+}$ in 88% and 69% isolated yield (Scheme 1), respectively.

Scheme 1. Synthesis of 3-$Al(OR_F)_4$ and 3-$(Al(OR_F)_4)_2$ by Oxidation of 3 with $Ag[Al(OR_F)_4]$ (R_F = $C(CF_3)_3$)

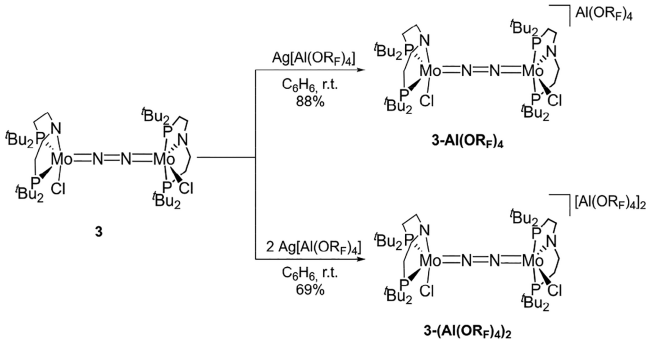

While Krossing's anion proved beneficial to obtain high yields in analytical purity, the crystallographic characterization of 3-$Al(OR_F)_4$ and 3-$(Al(OR_F)_4)_2$ was hampered by heavy disorder of the aluminate anions. Synthesis of the BF_4^- (**3**-$\mathbf{BF_4}$) and SbF_6^- (**3**-$(\mathbf{SbF_6})_2$) salts from oxidation with the respective silver reagents gave crystals that were suitable for XRD (Figure 3). The molecular structures of **3**-$\mathbf{BF_4}$ and **3**-$(\mathbf{SbF_6})_2$ strongly reflect those of parent **3** and the tungsten and rhenium analogues **4**/$\mathbf{4}^+$/$\mathbf{4}^{2+}$ and **2**.[8b,9,10] The approximately linearly bridging μ^2:η_1:η_1-N_2 ligands are sited in the apical positions of square-pyramidally coordinated Mo ions. The two pincer groups are twisted with respect to each other by 89.79(16)° (**3**-$\mathbf{BF_4}$) and 92.7(4)° (**3**-$(\mathbf{SbF_6})_2$), respectively, presumably due to steric crowding of the bulky *t*Bu substituents. The bond metrics within the {Mo−N−N−Mo} core of the series **3**/**3**-$\mathbf{BF_4}$/**3**-$(\mathbf{SbF_6})_2$ show insignificant changes (Table 1). For example, the N−N distances range between 1.237(5) (**3**-$\mathbf{BF_4}$) and 1.258(9) Å (**3**), and the Mo−N bonds range from 1.810(8) (**3**-$(\mathbf{SbF_6})_2$) to 1.799(4) (**3**). Similar observations were made for the respective tungsten series **4**/$\mathbf{4}^+$/$\mathbf{4}^{2+}$. Notably, the bond lengths around the two Mo ions of **3**-$\mathbf{BF_4}$ show small but significant differences (Mo1−Cl1 2.3519(11) Å, Mo2−Cl2 2.4515(11) Å), indicating valence localization within the mixed-valent complex in the solid state.

The room temperature EPR spectrum of low-spin complex 3-$Al(OR_F)_4$ in THF features a signal with an isotropic g value of 1.93, closely resembling that of tungsten analog $\mathbf{4}^+$ (g_{iso} = 1.90). Hyperfine coupling to only one of the molybdenum ions ($A(^{95/97}Mo)$ = 142 MHz) and two pincer phosphorus atoms ($A(^{31}P)$ = 33.7 MHz) is observed, supporting valence localization. In contrast, the number of ^1H NMR signals of paramagnetic 3-$Al(OR_F)_4$ at r.t. supports C_2 symmetry, suggesting delocalization on the slow NMR time scale. The spectroscopic characterization is therefore in agreement with a Robin-Day Class II classification.[27] Transition from the valence delocalized limit to weak electronic coupling was previously

https://dx.doi.org/10.1021/acs.inorgchem.0c02134
Inorg. Chem. 2020, 59, 14367−14375

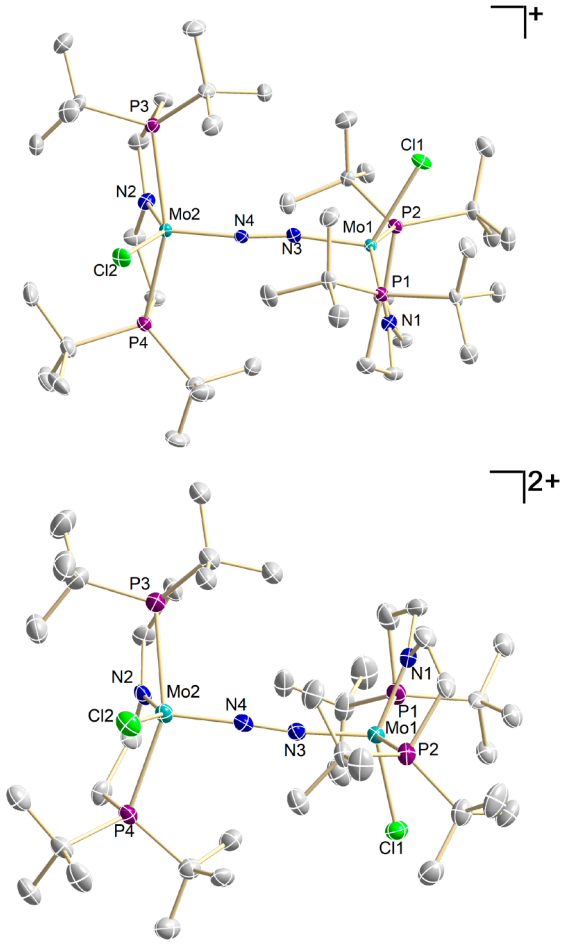

Figure 3. Molecular structures of $\mathbf{3}^{+}$-$\mathbf{BF_4}$ (top) and $\mathbf{3}^{2+}$-$(\mathbf{SbF_6})_2$ (bottom) from single-crystal XRD (thermal ellipsoids drawn at the 50% probability level); solvent molecules, anions, and hydrogen atoms are omitted for clarity. Selected bond lengths [Å] and angles [deg]: **3-BF$_4$**: Mo1−Cl1 2.3519(11), Mo1−N1 1.974(4), Mo1−N3 1.804(4), Mo1−P1 2.5387(12), Mo1−P2 2.5387(12), Mo2−Cl2 2.4515(11), Mo2−N2 1.974(4), Mo2−N4 1.825(4), Mo2−P3 2.4966(12), Mo2−P4 2.4921(12), N3−N4 1.237(5), N1−Mo1−N3 113.24(17), P1−Mo1−P2 155.84(4), Mo1−N3−N4 169.6(3), N2−Mo2−N4 109.51(16), P3−Mo2−P4 154.34(4), Mo2−N4−N3 170.9(3). **3-(SbF$_6$)$_2$**: Mo1−Cl1 2.352(3), Mo1−N1 1.958(8), Mo1−N3 1.803(8), Mo1−P1 2.532(3), Mo1−P2 2.583(3), Mo2−Cl2 2.349(3), Mo2−N2 1.963(8), Mo2−N4 1.810(8), Mo2−P3 2.534(3), Mo2−P4 2.574(3), N3−N4 1.253(11), N1−Mo1−N3 108.9(3), P1−Mo1−P2 151.29(9), Mo1−N3−N4 171.0(7), N2−Mo2−N4 108.1(3), P3−Mo2−P4 152.10(9), Mo2−N4−N3 168.7(7).

described by Meyer and co-workers for a series of linearly N_2 bridged, mixed-valent Os^{II}/Os^{III} complexes.[28]

The number of ^{1}H NMR resonances of two-electron oxidized product **3-(Al(OR$_F$)$_4$)$_2$** supports the preservation of C_2-symmetry in solution. All signals are paramagnetically broadened and shifted, suggesting thermal population of an open-shell state. As in the case of **3-Al(OR$_F$)$_4$**, ^{31}P signals were not found. The magnetic properties were examined by SQUID magnetometry. The $\chi_M T$ product of about 0.6 $cm^3 \cdot mol^{-1} \cdot K^{-1}$ drops to close to zero upon cooling to ca. 25 K indicating that the two spin centers are weakly coupled via the N_2 bridge. The magnetic data could be fitted with an effective Heisenberg−Dirac-van Vleck Hamiltonian ($\hat{H} = -2J\hat{S}_1\,\hat{S}_2 + g\mu_B\vec{B}\,(\vec{S}_1+\vec{S}_2)$) for two low-spin Mo^{III} ions (S = 1/2 each) that are weakly antiferromagnetically coupled via the N_2 bridge (J = −76 cm^{-1}).

The weak electronic coupling of the molybdenum ion in mixed valent **3-Al(OR$_F$)$_4$** and two-electron oxidized **3-(Al(OR$_F$)$_4$)$_2$** is consistent with the removal of electrons from the δ-symmetric orbitals (Figure 1), which are orthogonal to the σ- and π-MO manifold of the Mo−N−N−Mo bridge. Further support is provided by the degree of N_2 activation, as estimated by resonance Raman spectroscopy. Notably, **3-Al(OR$_F$)$_4$** and **3-(Al(OR$_F$)$_4$)$_2$** exhibit multiple bands in the spectral region around 1400 cm^{-1}, which is tentatively attributed to mixing of the N−N stretch with vibrational modes of the pincer backbone preventing an unequivocal assignment. However, the $^{15}N_2$ isotopologues feature isolated Raman bands, respectively. The $^{15}N_2$ stretching vibrations within the redox series are almost invariant upon oxidizing **3** ($\pi^8\delta^4$: ν_{NN} = 1300 cm^{-1}) to **3-Al(OR$_F$)$_4$** ($\pi^8\delta^3$: ν_{NN} = 1349 cm^{-1}) and **3-(Al(OR$_F$)$_4$)$_2$** ($\pi^8\delta^2$: ν_{NN} = 1343 cm^{-1}), respectively. The same observations were made for the isovalent tungsten redox series (Table 1). In comparison, oxidation of **1** (π^{10}) to $\mathbf{1}^{2+}$ (π^8) is associated with a significant bathochromic shift of $\Delta\nu$ = 281 cm^{-1}.

The electronic ground-state assignment for the Mo redox series $\mathbf{3}^{n+}$ (n = 0−2; Table 1) is further corroborated by DFT computations. Oxidation of **3** to valence localized $\mathbf{3}^{+}$ lifts the degeneracy of the δ-MOs and reproduces the experimentally observed structural distortion along the Mo−N−N−Mo axis. For the second oxidation product $\mathbf{3}^{2+}$, two almost degenerate (ΔG = 0.5 kcal mol^{-1}) lowest energy states were obtained, i.e., a triplet (T) state and an antiferromagnetically coupled (J_{DFT} = −196 cm^{-1}), open-shell singlet configuration (OSS). The calculated spin density distributions for $\mathbf{3}^{+}$ and $\mathbf{3}^{2+}$ (for both the T and OSS states) confirm the notion of metal centered, δ-MO based redox steps, that lead to $\{\pi^8\delta^3\}$ ($\mathbf{3}^{+}$) and $\{\pi^8\delta^2\}$ ($\mathbf{3}^{2+}$) configurations, respectively. Importantly, the relevant computed observables for this study, such as structural parameters, electronic coupling, and redox-induced shifts of the vibrational data, are satisfactorily reproduced.

X-ray Absorption Spectroscopy. The N_2 bridged reference complexes **3**, **3-Al(OR$_F$)$_4$**, and **3-(Al(OR$_F$)$_4$)$_2$**, the transient protonation product $\mathbf{3}^{2H+}$, and the product from protonation-induced N_2 splitting **5** were characterized by Mo K-edge X-ray absorption spectroscopy. The experiments were carried out in frozen THF under an atmosphere of Ar to avoid complications from coordination of additional N_2 to the coordinatively unsaturated complexes. The protonation product $\mathbf{3}^{2H+}$ was prepared *in situ* by protonation of **3** with triflic acid (2.5 equiv) at −80 °C prior to XAS characterization.

The Mo K-edge XANES of all five complexes display broad edges (see the SI), as typically observed for such high energy transitions due to short hole lifetimes (Figure S8). All five complexes feature main edge energies within <1 eV, reflecting close effective charges at the metal ions as a result of highly covalent bonding, which evens out (formal) metal redox states. In accord, distinct pre-edge features are observed for all compounds, that may arise from 4d mixing with ligand p orbitals. Strong enhancement of the formally dipole forbidden 1s→4d transition is also observed, e.g., for terminal Mo oxo complexes as an expression of short and strongly covalent Mo═O bonding.[11b,c] Accordingly, the pre-edge feature of nitrido complex **5** (d_{MoN}^{XRD} = 1.65 Å)[9] is considerably higher in intensity as compared with $\mathbf{3}^{n+}$ (d_{MoN}^{XRD} = 1.80−1.83 Å) and $\mathbf{3}^{2H+}$, which allows for distinguishing the protonated

https://dx.doi.org/10.1021/acs.inorgchem.0c02134
Inorg. Chem. 2020, 59, 14367−14375

Table 1. Comparison of Spectroscopic and Structural Features of Linearly N_2 Bridged PNP Pincer Complexes (PNP′ = N(CHCHP*t*Bu$_2$)$_2$)

compound	electronic configuration	charge	$\nu(^{14}N_2)$[a]/cm^{-1}	d(NN)/Å
1	$\{\pi^{10}\}$	2	1630 (1577)	1.212(2)/1.217(2)
1^{+}	$\{\pi^{9}\}$	1	1503 (1438)	1.239(4)
1^{2+}	$\{\pi^{8}\}$	0	1349 (1305)	1.265(5)
2	$\{\pi^{10}\delta^{4}\}$	2	1771[b]	1.202(10)
3	$\{\pi^{8}\delta^{4}\}$	0	1343 (1300)	1.258(9)
3-Al(OR$_F$)$_4$	$\{\pi^{8}\delta^{3}\}$	1	1390−1405[c] (1349)	1.237(5)
3-(Al(OR$_F$)$_4$)$_2$	$\{\pi^{8}\delta^{2}\}$	2	1382−1406[c] (1343)	1.253(11)
4	$\{\pi^{8}\delta^{4}\}$	0	1392 (1347)	1.33(4)/1.27(8)
4^{+}	$\{\pi^{8}\delta^{3}\}$	1	1414 (1360)	1.277(5)
4^{2+}	$\{\pi^{8}\delta^{2}\}$	2	1400 (1356)	1.266(12)
[N$_2${Ir(PNP′)}$_2$]	$\{\pi^{12}\delta^{8}\}$	0	2003[b]	1.135(4)
[N$_2${Ir(PNP′)}$_2$]$^{+}$	$\{\pi^{11}\delta^{8}\}$	1	1960	1.136(6)
[N$_2${Ir(PNP′)}$_2$]$^{2+}$	$\{\pi^{10}\delta^{8}\}$	2	1989[b]	1.138(6)

[a]Values for the $^{15}N_2$ isotopologues are given in parentheses. [b]Computed. [c]Multiplet.[6,8−10,29]

intermediate from the N−N splitting product spectroscopically. Warming of an *in situ* prepared sample of **3**$^{2H+}$ to r.t. results in a sharp rise of the pre-edge feature and essentially quantitative reproduction of the spectrum of **5**, supporting the spectroscopic assignment.

The same trend with respect to the intensity of the pre-edge feature was reported by Laplaza et al. for **1** and the nitrido splitting product [Mo(N)(NRAr)$_3$].[6b] Notably, Yamamoto et al. did not observe a pre-edge peak upon *in situ* reduction of the pyridine-based Mo^{III} pincer complex [MoI$_3$(PNP′′)] (PNP′′ = NC$_5$H$_3$-2,6-CH$_2$P*t*Bu$_2$) under N_2 at 198 K.[12] The authors related this observation to symmetry arguments, namely the formation of octahedral dinitrogen products, i.e., either [MoI(N$_2$)$_2$(PNP″)] or [(μ^2:η^1:η^1-N$_2$){MoI(N$_2$)-(PNP″)}$_2$, and therefore reduced 4d/5p mixing. However, Mo−Mo scattering that unequivocally confirms the formation of dinuclear N_2 activation products could not be found in the EXAFS part of the spectrum.

The EXAFS parts of the Mo−K edge spectra of the independently synthesized and structurally well-defined dinuclear complexes **3**, **3-Al(OR$_F$)$_4$**, and **3-(Al(OR$_F$)$_4$)$_2$** and the final nitride product **5** were analyzed and compared with **3**$^{2H+}$ to obtain structural information about the transient protonation product. Selected bond lengths are presented in Table 2 (for full EXAFS data analyses results see Figures S9−S13 of the SI). The bond lengths derived for the N_2 bridged reference set from EXAFS analysis reproduce the structural parameters obtained from single-crystal XRD within experimental error (3σ). The only significant difference is given by the Mo−N$_{PNP}$ bond length of **3** which is about 0.07 Å longer from XAS. This outlier is tentatively attributed to crystallographic disorder of **3** in the solid state that arises from superimposition of two {MoCl(PNP)} fragment conformers.[9] Note that the DFT computed value is in excellent agreement with the EXAFS model. A clear trend is obtained for the Mo−Cl bond along the redox series **3**/**3-Al(OR$_F$)$_4$**/**3-(Al(OR$_F$)$_4$)$_2$**. Upon oxidation, the distance gradually shortens to stabilize the metal centered oxidations, which, in turn, proceed under retention of the edge energy as discussed above. The XAS derived bond lengths are also nicely reproduced by DFT. Only the computed Mo−Mo distances are slightly shorter by around 0.1 Å in all cases, which can be attributed to slight deviations of the Mo−N−N−Mo core from linearity as applied in the EXAFS model. For the nitride complex **5**, a significantly shorter Mo≡N bond length was obtained by EXAFS compared with XRD and DFT, which may be attributed to perturbation of triflate anion coordination to the protonated pincer ligand in solution.

The EXAFS spectrum of *in situ* generated **3**$^{2H+}$ could be fitted satisfactorily as a dimeric Mo dinitrogen complex with small amounts of the splitting product **5** (Figure 4). However, the estimate for the Mo−Mo distance as a key structural parameter (see below) is not affected by impurities from the mononuclear nitride. Comparison of **3**$^{2H+}$ with the structural data of the reference compounds shows several differences (Table 2). The Mo−N$_{PNP}$ distance is significantly longer than in **3**$^{n+}$ (n = 0−2), which is consistent with the absence of N→Mo π-donation upon N-protonation of the amide ligands. Furthermore, the Mo−N_2 distance also increases as is expected for the population of the (π^*−π−π^*) MOs (Figure 1) due to a transition from S = 0 (**3**) to a higher spin state (Figure 2). In consequence, the Mo−Mo distance is sharply increased by around 0.3 Å, as derived from the distinct Mo−Mo multiple scattering pathway that could be identified (d_{Mo-Mo} = 5.17(3) Å).

The electronic ground-state assignment was further evaluated upon comparison of the EXAFS data of **3**$^{2H+}$ with computed structures for the singlet (S = 0), triplet (S = 1), and quintet (S = 2) states that had been previously reported. The low-spin state exhibits a ($\pi^8\delta^4$) configuration. The ($\pi^{10}\delta^2$) high-spin and intermediate-spin configurations are closely related with antiferromagnetic coupling of the two unpaired δ-electrons across the N_2 bridge in the triplet electromer. Rescaling of the previously reported free energies for the experimental XAS conditions (100 K)[9] predicts the quintet as ground state below the singlet ($\Delta G^{100\,K}$ = +5.5 kcal·mol^{-1}) and triplet ($\Delta G^{100\,K}$ = +5.8 kcal·mol^{-1}) states. The most prominent structural marker for the computed spin states is the Mo−Mo distance (Table 2), which is considerably shorter for the singlet state by about 0.2 Å due to stronger Mo−N bonding (see above). Considering a slight overestimation of the Mo−Mo distance of ca. 0.1 A by the EXAFS model (see above), the computated values for the quintet and triplet states are in excellent agreement. The high- and intermediate-spin states cannot be distinguished from structural data due to their closely related electronic configurations (see above). However, the EXAFS study unequivocally supports the previously proposed protonation-induced transition from S = 0 to a

https://dx.doi.org/10.1021/acs.inorgchem.0c02134
Inorg. Chem. 2020, 59, 14367−14375

Table 2. Comparison of Selected Structural Parameters Derived by X-ray Diffraction (XRD), X-ray Absorption Spectroscopy (XAS), and DFT Calculations

	Mo−N_{PNP}/Å			Mo−N/Å[a]			N−N/Å			Mo−Mo/Å			Mo−Cl/Å	
	XRD	XAS	DFT	XRD	XAS	DFT	XRD	XAS	DFT	XRD	XAS	DFT	XRD	XAS	DFT
3[b]	1.917(7)	1.99(2)	1.99	1.799(4)	1.80(1)	1.79	1.258(9)	1.21(3)	1.24	4.846(1)	4.90(2)	4.80	2.595(7)	2.43(1)	2.46
3-Al(OR$_F$)$_4$	1.974(4)	1.98(2)	1.99	1.804(4)	1.81(2)	1.81	1.237(5)	1.19(2)	1.22	4.846(1)	4.90(2)	4.81	2.3519(11)	2.42(2)	2.43
	1.974(4)		1.97	1.825(4)		1.77							2.4515(11)		2.37
3-(Al(OR$_F$)$_4$)$_2$	1.958(8)	1.93(3)	1.97	1.803(8)	1.81(2)	1.79	1.253(11)	1.18(3)	1.22	4.847(2)	4.87(1)	4.80	2.352(2)	2.36(2)	2.34
	1.963(8)			1.810(8)									2.349(3)		
5[9]	2.209(2)	2.11(3)	2.29	1.646(2)	1.62(1)	1.69							2.3763(5)	2.37(1)	

	Mo−N_{PNP}/Å			Mo−N/Å[a]			N−N/Å			Mo−Mo/Å			Mo−Cl/Å		
3^{2H+9}	XAS	DFT		XAS	DFT		XAS	DFT		XAS	DFT		XAS	DFT	
S = 0		2.30			1.82			1.27			4.88			2.52	
S = 1		2.34			1.93			1.22			5.05			2.50	
S = 2		2.32			1.94			1.22			5.08			2.50	
exp	2.30(9)		1.87(2)			n.a.			5.17(3)			2.48(6)			

[a]Mo−N denotes the distance of the metal atom to either the N_2 or the nitrido ligands. [b]The computational model for **3** was reoptimized and therefore slightly deviates from the value reported in ref 9.

higher spin state with ($\pi^{10}\delta^2$) configuration prior to facile splitting of the N−N bond.

CONCLUSIONS

In summary, an *in situ* XAS study was presented to evaluate our previous proposal that the protonation-induced splitting of singlet **3** into nitrido complex **5** is associated with a spin transition prior to N−N cleavage. XANES data for the {Mo_2N_2} redox series **3**/**3**$^+$/**3**$^{2+}$ and terminal nitride **5** as the reference set, as well as the protonated key intermediate **3**$^{2H+}$, indicate highly covalent bonding, as is typically observed, e.g., for oxo complexes. EXAFS analysis confirms a considerable elongation of the {Mo−N−N−Mo} core as a result of protonation of the PNP pincer backbone of **3**. This observation is consistent with the previously proposed transition to a product with ($\pi^{10}\delta^2$) configuration (Figure 2) and S = 1 or S = 2 ground state, which is thermally unstable with respect to N−N cleavage. The high- and intermediate-spin states of **3**$^{2H+}$ are electronically closely related and derived from the singlet by population of the ($\pi^*-\pi-\pi^*$) levels of the {Mo−N−N−Mo} core from nonbonding δ orbitals. Computational analysis favors the quintet as ground state by about 5 kcal·mol^{-1}.

This work supports the simple model that the accessibility of ($\pi^{10}\delta^*$) states (Figure 1) is a prerequisite for the splitting of linearly N_2 bridged, dinuclear complexes into terminal nitrides. It further demonstrates how small variations of the auxiliary ligand field can be utilized to control the kinetics of N_2 splitting.

ASSOCIATED CONTENT

Supporting Information

The Supporting Information is available free of charge at https://pubs.acs.org/doi/10.1021/acs.inorgchem.0c02134.

Spectroscopic, magnetic, and computational data of **3**, **3-Al(OR$_F$)$_4$** and **3-(Al(OR$_F$)$_4$)$_2$**, crystallographic details of **3-BF$_4$** and **3-(SbF$_6$)$_2$**, description of XAS measurements, XANES and EXAFS results of **3**, **3-Al(OR$_F$)$_4$**, **3-(Al(OR$_F$)$_4$)$_2$**, **5**, and protonation product **3**$^{2H+}$ (PDF)

Computed .xyz files of **3**, **3**$^+$, and **3**$^{2+}$ (ZIP)

Accession Codes

CCDC 2015019−2015020 contain the supplementary crystallographic data for this paper. These data can be obtained free of charge via www.ccdc.cam.ac.uk/data_request/cif, or by emailing data_request@ccdc.cam.ac.uk, or by contacting The Cambridge Crystallographic Data Centre, 12 Union Road, Cambridge CB2 1EZ, UK; fax: +44 1223 336033.

AUTHOR INFORMATION

Corresponding Authors

Sven Schneider − *Institut für Anorganische Chemie, Georg-August-Universität Göttingen, 37077 Göttingen, Germany;* orcid.org/0000-0002-8432-7830; Email: sven.schneider@chemie.uni-goettingen.de

Moniek Tromp − *Faculty of Science and Engineering, University of Groningen, 9747 AG Groningen, The Netherlands;* orcid.org/0000-0002-7653-1639; Email: moniek.tromp@rug.nl

https://dx.doi.org/10.1021/acs.inorgchem.0c02134
Inorg. Chem. 2020, 59, 14367−14375

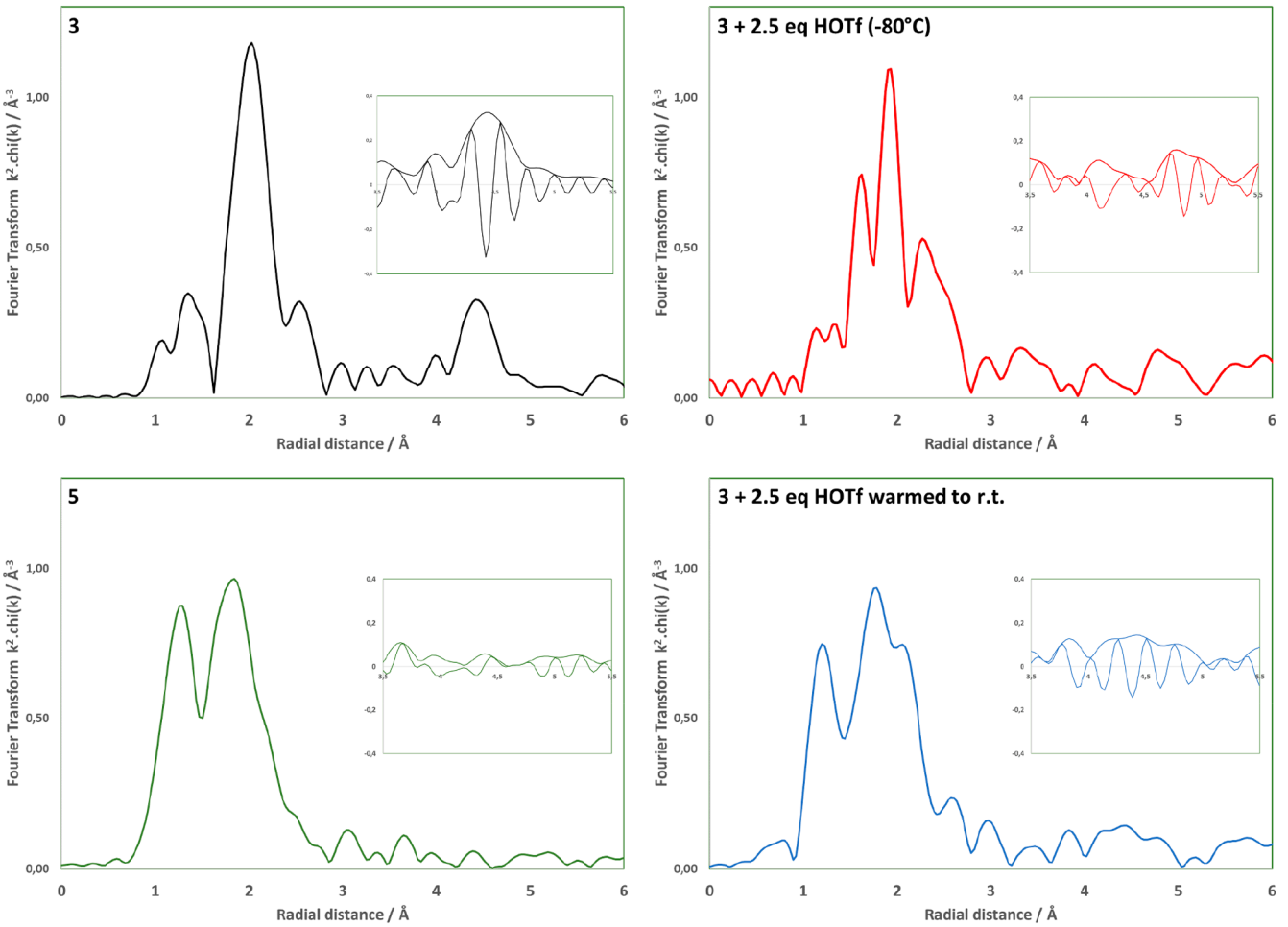

Figure 4. k^2 weighted Fourier transform of the Mo K-edge EXAFS data of **3** (black), the product of **3** and 2.5 equiv of triflic acid at −80 °C (red) and after warming to room temperature (blue), and of independently synthesized **5** (green). The insets show enlargements of the 3.5−5 Å regions overlaid with the imaginary parts of the spectrum.

Authors

Josh Abbenseth − *Institut für Anorganische Chemie, Georg-August-Universität Göttingen, 37077 Göttingen, Germany;* orcid.org/0000-0002-8787-6253

Jean-Pierre H. Oudsen − *Van't Hoff Institute for Molecular Sciences (HIMS), University of Amsterdam, 1098XH Amsterdam, The Netherlands*

Bas Venderbosch − *Van't Hoff Institute for Molecular Sciences (HIMS), University of Amsterdam, 1098XH Amsterdam, The Netherlands*

Serhiy Demeshko − *Institut für Anorganische Chemie, Georg-August-Universität Göttingen, 37077 Göttingen, Germany*

Markus Finger − *Institut für Anorganische Chemie, Georg-August-Universität Göttingen, 37077 Göttingen, Germany*

Christian Herwig − *Institut für Chemie, Humboldt Universität zu Berlin, 12489 Berlin, Germany*

Christian Würtele − *Institut für Anorganische Chemie, Georg-August-Universität Göttingen, 37077 Göttingen, Germany*

Max C. Holthausen − *Institut für Anorganische und Analytische Chemie, Goethe-Universität, 60438 Frankfurt am Main, Germany;* orcid.org/0000-0001-7283-8329

Christian Limberg − *Institut für Chemie, Humboldt Universität zu Berlin, 12489 Berlin, Germany;* orcid.org/0000-0002-0751-1386

Complete contact information is available at: https://pubs.acs.org/10.1021/acs.inorgchem.0c02134

Author Contributions

[#]J.-P.H.O. and B.V. contributed equally.

Notes

The authors declare no competing financial interest.

■ ACKNOWLEDGMENTS

M. Fritz is acknowledged with help for the crystallographic data acquisition. The authors are grateful to the European Research Council (S.S.; ERC Grant Agreement 646747) and the Fonds der Chemischen Industrie (FCI Doktoranden Stipendium for J.A.) for financial support and NWO (VIDI grant 723.014.010 to M.T.; for M.T., B.V., J.P.O.) for funding. The Diamond Light Source is gratefully acknowledged for beamtime under proposal number SP22432.

■ REFERENCES

(1) Schlögl, R. In *Handbook of Heterogeneous Catalysis*; Ertl, G., Knözinger, H., Schüth, F., Weitkamp, J., Eds.; Wiley-VCH: Weinheim, 2008; Vol. 5, pp 2501−2575.

(2) Foster, S. L.; Perez Bakovic, S. I.; Duda, R. D.; Maheshwari, S.; Milton, R. D.; Minteer, S. D.; Janik, M. J.; Renner, J. N.; Greenlee, L. F. Catalysts for nitrogen reduction to ammonia. *Nature Catal.* **2018**, *1*, 490−500.

(3) Hoffman, B. M.; Lukoyanov, D.; Yang, Z.-Y.; Dean, D. R.; Seefeldt, L. C. Mechanism of Nitrogen Fixation by Nitrogenase: The Next Stage. *Chem. Rev.* **2014**, *114*, 4041−4062.
(4) Chalkley, M. J.; Drover, M. W.; Peters, J. C. Catalytic N_2-to-NH_3 (or -N_2H_4) Conversion by Well-Defined Molecular Coordination Complexes. *Chem. Rev.* **2020**, *120*, 5582−5636.
(5) (a) Arashiba, K.; Eizawa, A.; Tanaka, H.; Nakajima, K.; Yoshizawa, K.; Nishibayashi, Y. Catalytic Nitrogen Fixation via Direct Cleavage of Nitrogen−Nitrogen Triple Bond of Molecular Dinitrogen under Ambient Reaction Conditions. *Bull. Chem. Soc. Jpn.* **2017**, *90*, 1111−1118. (b) Ashida, Y.; Arashiba, K.; Nakajima, K.; Nishibayashi, Y. Molybdenum-catalysed ammonia production with samarium diiodide and alcohols or water. *Nature* **2019**, *568*, 536−540.
(6) (a) Laplaza, C. E.; Cummins, C. C. Dinitrogen Cleavage by a Three-Coordinate Molybdenum(III) Complex. *Science* **1995**, *268*, 861−863. (b) Laplaza, C. E.; Johnson, M. J. A.; Peters, J. C.; Odom, A. L.; Kim, E.; Cummins, C. C.; George, G. N.; Pickering, I. J. Dinitrogen Cleavage by Three-Coordinate Molybdenum(III) Complexes: Mechanistic and Structural Data. *J. Am. Chem. Soc.* **1996**, *118*, 8623−8638.
(7) Klopsch, I.; Yuzik-Klimova, E.; Schneider, S. Functionalization of N_2 by Mid to Late Transition Metals via N−N Bond Cleavage. *Top. Organomet. Chem.* **2017**, *60*, 71−112.
(8) (a) Klopsch, I.; Finger, M.; Würtele, C.; Milde, B.; Werz, D. B.; Schneider, S. Dinitrogen Splitting and Functionalization in the Coordination Sphere of Rhenium. *J. Am. Chem. Soc.* **2014**, *136*, 6881−6883. (b) Lindley, B. M.; van Alten, R. S.; Finger, M.; Schendzielorz, F.; Würtele, C.; Miller Miller, A. J. M.; Siewert, I.; Schneider, S. Mechanism of Chemical and Electrochemical N_2 Splitting by a Rhenium Pincer Complex. *J. Am. Chem. Soc.* **2018**, *140*, 7922−7935.
(9) Silantyev, G. A.; Förster, M.; Schluschaß, B.; Abbenseth, J.; Würtele, C.; Volkmann, C.; Holthausen, M. C.; Schneider, S. Dinitrogen Splitting Coupled to Protonation. *Angew. Chem., Int. Ed.* **2017**, *56*, 5872−5876.
(10) Schluschaß, B.; Abbenseth, J.; Demeshko, S.; Finger, M.; Franke, A.; Herwig, C.; Würtele, C.; Ivanovic-Burmazovic, I.; Limberg, C.; Telser, J.; Schneider, S. Selectivity of tungsten mediated dinitrogen splitting vs. proton reduction. *Chem. Sci.* **2019**, *10*, 10275−10282.
(11) (a) Cramer, S. P.; Hodgson, K. O.; Stiefel, E. I.; Newton, W. E. A Systematic X-Ray Absorption Study of Molybdenum Complexes. The Accuracy of Structural Information from Extended X-Ray Absorption Fine Structure. *J. Am. Chem. Soc.* **1978**, *100*, 2748−2761. (b) Pushie, M. J.; George, G. N. Spectroscopic Studies of Molybdenum and Tungsten Enzymes. *Coord. Chem. Rev.* **2011**, *255*, 1055−1084. (c) Lima, F. A.; Bjornsson, R.; Weyhermüller, T.; Chandrasekaran, P.; Glatzel, P.; Neese, F.; DeBeer, S. High-resolution molybdenum K-edge X-ray absorption spectroscopy analyzed with time-dependent density functional theory. *Phys. Chem. Chem. Phys.* **2013**, *15*, 20911−20920. (d) Tromp, M. Catalysis Seen in Action. *Philos. Trans. R. Soc., A* **2015**, *373*, 20130152. (e) Kowalska, J.; DeBeer, S. The role of X-ray spectroscopy in understanding the geometric and electronic structure of nitrogenase. *Biochim. Biophys. Acta, Mol. Cell Res.* **2015**, *1853*, 1406−1415. (f) Van Stappen, C.; Decamps, L.; Cutsail, G. E., III; Bjornsson, R.; Henthorn, J. T.; Rirrell, J. A.; DeBeer, S. The Spectroscopy of Nitrogenases. *Chem. Rev.* **2020**, *120*, 5005−5081.
(12) Yamamoto, A.; Arashiba, K.; Naniwa, S.; Kato, K.; Tanaka, H.; Yoshizawa, K.; Nishibayashi, Y.; Yoshida, H. Structural characterization of molybdenum− dinitrogen complex as key species toward ammonia formation by dispersive XAFS spectroscopy. *Phys. Chem. Chem. Phys.* **2020**, *22*, 12368−12372.
(13) Stoll, S.; Schweiger, A. Easyspin, a comprehensive software package for spectral simulation and analysis of EPR. *J. Magn. Reson.* **2006**, *178*, 42−55.
(14) Haberditzl, W. Advances in Molecular Diamagnetism. *Angew. Chem., Int. Ed. Engl.* **1966**, *5*, 288−298.
(15) Bill, E. *julX*, Program for Simulation of Molecular Magnetic Data; 2008.
(16) (a) *APEX3* v2016.9-0 (SAINT/SADABS/SHELXT/SHELXL); Bruker AXS Inc.: Madison, WI, USA, 2016. (b) Sheldrick, G. M. SHELXT - Integrated space-group and crystal-structure determination. *Acta Crystallogr., Sect. A: Found. Adv.* **2015**, *A71*, 3−8. (c) Sheldrick, G. M. Crystal structure refinement with SHELXL. *Acta Crystallogr., Sect. C: Struct. Chem.* **2015**, *C71*, 3−8. (d) Sheldrick, G. M. A short history of SHELX. *Acta Crystallogr., Sect. A: Found. Crystallogr.* **2008**, *A64*, 112−122.
(17) (a) Neese, F. The ORCA program system. *Wiley Interdiscip. Rev.: Comput. Mol. Sci.* **2012**, *2*, 73−78. (b) Neese, F. Software update: the ORCA program system, version 4.0. *Wiley Interdiscip. Rev.: Comput. Mol. Sci.* **2018**, *8*, e1327.
(18) Adamo, C.; Barone, V. Toward reliable density functional methods without adjustable parameters: The PBE0 model. *J. Chem. Phys.* **1999**, *110* (110), 6158−6170.
(19) (a) Grimme, S.; Antony, J.; Ehrlich, S.; Krieg, H. A consistent and accurate ab initio parametrization of density functional dispersion correction (DFT-D) for the 94 elements H-Pu. *J. Chem. Phys.* **2010**, *132*, 154104. (b) Grimme, S.; Ehrlich, S.; Goerigk, L. Effect of the damping function in dispersion corrected density functional theory. *J. Comput. Chem.* **2011**, *32*, 1456−1465.
(20) Neese, F.; Wennmohs, F.; Hansen, A.; Becker, U. Robust fitting techniques in the chain of spheres approximation to the Fock exchange: The role of the complementary space. *Chem. Phys.* **2009**, *356*, 98−109.
(21) (a) Eichkorn, K.; Weigend, F.; Treutler, O.; Ahlrichs, R. Auxiliary basis sets for main row atoms and transition metals and their use to approximate Coulomb potentials. *Theor. Chem. Acc.* **1997**, *97*, 119−124. (b) Andrae, D.; Haeussermann, U.; Dolg, M.; Stoll, H.; Preuss, H. Energy-adjusted ab initio pseudopotentials for the second and third row transition elements. *Theor. Chim. Acta* **1990**, *77*, 123−141. (c) Weigend, F.; Ahlrichs, R. Balanced basis sets of split valence, triple zeta valence and quadruple zeta valence quality for H to Rn: Design and assessment of accuracy. *Phys. Chem. Chem. Phys.* **2005**, *7*, 3297−3305. (d) Weigend, F.; Häser, M.; Patzelt, H.; Ahlrichs, R. RI-MP2: optimized auxiliary basis sets and demonstration of efficiency. *Chem. Phys. Lett.* **1998**, *294*, 143−152.
(22) (a) Soda, T.; Kitagawa, Y.; Onishi, T.; Takano, Y.; Shigeta, Y.; Nagao, H.; Yoshioka, Y.; Yamaguchi, K. Ab initio computations of effective exchange integrals for H-H, H-He-H and Mn_2O_2 complex: comparison of broken-symmetry approaches. *Chem. Phys. Lett.* **2000**, *319*, 223−230. (b) Yamanaka, S.; Kawakami, T.; Nagao, H.; Yamaguchi, K. Effective exchange integrals for open-shell species by density functional methods. *Chem. Phys. Lett.* **1994**, *231*, 25−33. (c) Knijnenburg, Q.; Hetterscheid, D.; Kooistra, T. M.; Budzelaar, P. H. M. The Electronic Structure of (Diiminopyridine)cobalt(I) Complexes. *Eur. J. Inorg. Chem.* **2004**, *2004*, 1204−1211.
(23) Zhao, Y.; Truhlar, D. G. The M06 suite of density functionals for main group thermochemistry, thermochemical kinetics, noncovalent interactions, excited states, and transition elements: two new functionals and systematic testing of four M06-class functionals and 12 other functionals. *Theor. Chem. Acc.* **2008**, *120*, 215−241.
(24) Marenich, A. V.; Cramer, C. J.; Truhlar, D. G. Universal solvation model based on solute electron density and on a continuum model of the solvent defined by the bulk dielectric constant and atomic surface tensions. *J. Phys. Chem. B* **2009**, *113*, 6378−6396.
(25) Grimme, S. Supramolecular Binding Thermodynamics by Dispersion-Corrected Density Functional Theory. *Chem. - Eur. J.* **2012**, *18*, 9955−9964.
(26) Ravel, B.; Newville, M. ATHENA, ARTEMIS, HEPHAESTUS: data analysis for X-ray absorption spectroscopy using IFEFFIT. *J. Synchrotron Radiat.* **2005**, *12*, 537−541.
(27) Robin, M. B.; Day, P. Mixed Valence Chemistry-A Survey and Classification. *Adv. Inorg. Chem. Radiochem.* **1968**, *10*, 247−422.
(28) Demadis, K. D.; El-Sammanody, E.-S.; Coia, G. M.; Meyer, T. J. $Os^{III}(N_2)Os^{II}$ Complexes at the Localized-to-Delocalized, Mixed-Valence Transition. *J. Am. Chem. Soc.* **1999**, *121*, 535−544.

https://dx.doi.org/10.1021/acs.inorgchem.0c02134
Inorg. Chem. 2020, 59, 14367−14375

(29) Abbenseth, J.; Finger, M.; Würtele, C.; Kasanmascheff, M.; Schneider, S. Coupling of terminal iridium nitrido complexes. *Inorg. Chem. Front.* **2016**, *3*, 469−477.

https://dx.doi.org/10.1021/acs.inorgchem.0c02134
Inorg. Chem. 2020, 59, 14367−14375